

A study of the effects of a thermally evaporated nanoscale CsBr layer on the optoelectronic properties and stability of formamidinium-rich perovskite solar cells

Cite as: AIP Advances **11**, 095112 (2021); <https://doi.org/10.1063/5.0064398>

Submitted: 22 July 2021 • Accepted: 30 August 2021 • Published Online: 15 September 2021

 Richard K. Koech, Reysya Ichwani, Julia L. Martin, et al.



View Online



Export Citation



CrossMark

ARTICLES YOU MAY BE INTERESTED IN

[Annealing effects on interdiffusion in layered FA-rich perovskite solar cells](#)

AIP Advances **11**, 065327 (2021); <https://doi.org/10.1063/5.0046205>

[Pressure and thermal annealing effects on the photoconversion efficiency of polymer solar cells](#)

AIP Advances **11**, 045304 (2021); <https://doi.org/10.1063/5.0045694>

[Pressure-assisted fabrication of perovskite light emitting devices](#)

AIP Advances **11**, 025112 (2021); <https://doi.org/10.1063/5.0035953>

Call For Papers!

AIP Advances

SPECIAL TOPIC: Advances in
Low Dimensional and 2D Materials

A study of the effects of a thermally evaporated nanoscale CsBr layer on the optoelectronic properties and stability of formamidinium-rich perovskite solar cells

Cite as: AIP Advances 11, 095112 (2021); doi: 10.1063/5.0064398

Submitted: 22 July 2021 • Accepted: 30 August 2021 •

Published Online: 15 September 2021










View Online



Export Citation



CrossMark

Richard K. Koech,^{1,2,3}  Reisa Ichwani,² Julia L. Martin,⁴ Deborah O. Oyewole,^{2,5} 
Omolara V. Oyelade,⁶ Yusuf A. Olanrewaju,¹ Dahiru M. Sanni,⁶  Sharafadeen A. Adeniji,⁶ 
Ronald L. Grimm,⁴ Abdulhakeem Bello,¹  Oluwaseun K. Oyewole,^{2,5}  Esidor Ntsoenzok,⁷
and Winston O. Soboyejo^{2,5,8,a)} 

AFFILIATIONS

¹ Department of Materials Science and Engineering, African University of Science and Technology, P.M.B. 681, Garki-Abuja, Federal Capital Territory, Nigeria

² Department of Mechanical Engineering, Worcester Polytechnic Institute, 100 Institute Road, Worcester, Massachusetts 01609, USA

³ Department of Mathematic, Physics and Computing, Moi University, P.O. Box 3900-30100, Eldoret, Kenya

⁴ Department of Chemistry and Biochemistry, Life Science and Engineering Center, Worcester Polytechnic Institute, 100 Institute Road, Worcester, Massachusetts 01609, USA

⁵ Program in Materials Science and Engineering, Department of Mechanical Engineering, Worcester Polytechnic Institute, 100 Institute Road, Worcester, Massachusetts 01609, USA

⁶ Department of Theoretical and Applied Physics, African University of Science and Technology, P.M.B. 681, Garki-Abuja, Federal Capital Territory, Nigeria

⁷ CEMHTI-CNRS Site Cyclotron, 3A rue de la f erollerie, 45071 Orl ans, France

⁸ Department of Biomedical Engineering, Worcester Polytechnic Institute, Gateway Park Life Sciences and Bioengineering Center, 60 Prescott Street, Worcester, Massachusetts 01609, USA

^{a)} Author to whom correspondence should be addressed: wsoboyejo@wpi.edu. Current address: Program in Materials Science and Engineering, Worcester Polytechnic Institute, 100 Institute Road, Worcester, Massachusetts 01609, USA. Tel.: +1 508 831 5448

ABSTRACT

Incorporation of cesium (Cs) into the perovskite layer has become a good strategy to boost the stability and power conversion efficiency (PCE) of perovskite solar cells (PSCs). However, a suitable and scalable method of Cs incorporation in a perovskite film that does not cause a significant increase in the optical bandgap is needed. In this paper, we introduce a thin layer of CsBr into a formamidinium (FA)-rich mixed halide perovskite film using the thermal evaporation technique. The effects of the thickness of the CsBr layer on the microstructural, structural, and optoelectronic properties and surface chemical states of the perovskite film are then studied. The results indicate that the CsBr layer thickness is able to tune the microstructural and optoelectronic properties of the perovskite film. Planar PSCs fabricated with different thicknesses of CsBr layers in the perovskite absorber exhibited different photovoltaic performance characteristics. The CsBr-modified PSC device with a 50 nm layer of CsBr in the perovskite layer showed a better PCE of $16.19\% \pm 0.17\%$, which was about 15% higher than that of the control device, and was able to retain nearly 70% of its initial PCE value after 120 days of storage in an unencapsulated state.

© 2021 Author(s). All article content, except where otherwise noted, is licensed under a Creative Commons Attribution (CC BY) license (<http://creativecommons.org/licenses/by/4.0/>). <https://doi.org/10.1063/5.0064398>

I. INTRODUCTION

Perovskite solar cells (PSCs) are emerging solar cells with unique optoelectronic properties and simple processing routes that make them stand out from other photovoltaic (PV) technologies in the pursuit of high performance and low-cost solar energy harnessing systems.^{1–3} Within a short period of time, PSCs have achieved a remarkable progress in their power conversion efficiencies (PCEs) and are currently almost at par with the conventional PV technologies based on crystalline silicon.⁴ This progress was a culmination of many concerted efforts from researchers drawn from different disciplines that yielded a better understanding of their structure, optoelectronic properties, and their working principles.^{5,6} However, the PSC technology is still faced with myriads of challenges, which, among others, include non-radiative recombination power losses and performance degradation under the real outdoor operating conditions.^{7,8}

Various studies that have been carried out to probe the origin of the abovementioned challenges have pointed out that they are majorly caused by perovskite phase instability and the presence of defects in the bulk of the active layer and at the interfaces with the charge transport layers (CTLs).^{9–11} The morphology of the perovskite film plays a big role in controlling the defect states in the bulk and at the interfaces. Therefore, research efforts have been expended to improve the morphology of the perovskite active layer through compositional engineering,¹² solvent engineering,¹³ optimization of perovskite pre-cursors,¹⁴ additive engineering,¹⁵ improving deposition conditions,¹⁶ and optimization of post-treatment techniques.¹⁷ These strategies are aimed at controlling the nucleation and crystallization dynamics of the perovskite film with a view of passivating the defects at grain boundaries, which are the genesis of most problems in PSCs.^{18–20} The tunability of the perovskite (ABX₃) structure through elemental substitution and mixing has given rise to perovskite films with mixed cations and mixed halides, which have better morphologies and superior photophysical properties.^{12,21,22} The elemental substitution/mixing also tunes the tolerance factor that stabilizes the perovskite phase and improves its stability.^{23,24}

In an effort to enhance PCEs and stability of PSCs, cesium (Cs)-based mixed cation-mixed halide perovskite solar cells (PSCs) have been explored.^{25–27} The Cs atom occupies the A-site in the ABX₃ structure of perovskite, which is important in the formation of the close packed structure and in improving charge carrier mobility in perovskite films.²⁸ The ionic radii of the A-site cations control the B–X bond length in the perovskite structure, which dictates the bandgap of the resulting perovskite film.²⁹ The smaller ionic radius of Cs⁺ (1.81 Å) can cause lattice contraction or octahedral tilting, which increases the bandgap of the perovskite film.^{30,31} Despite this, the presence of Cs⁺ in the right proportion is beneficial in stabilizing the perovskite α -phase, reducing the defect density, as well as improving optical absorption and carrier lifetimes in the perovskite layer, which, in turn, improves the stability, reproducibility, and PCE of PSCs.^{26,27,32}

Cs⁺ is incorporated into the perovskite film from cesium halides (CsX, where X = I, Br, Cl), which are usually added directly into the precursor solutions or via the interfacial interdiffusion method.^{25,33,34} Recent studies have found the interfacial interdiffusion method to be a good strategy to incorporate Cs⁺ into the perovskite absorber layer while simultaneously tuning the interface energetics.³⁵ The technique can allow for localized incorporation of Cs⁺ within the vicinity of the interface between the perovskite layer and the charge transport layers (CTLs), which helps mitigate the expected blueshift in the absorption edge of the perovskite film while boosting its crystallization dynamics. Among the Cs halides, CsBr has been shown to be more effective in improving both the PCE and stability of PSCs.^{36–38} Pang *et al.*³⁹ incorporated CsBr into the perovskite film via the interfacial interdiffusion method, and they found that CsBr is essential in passivating the defects in perovskite bulk, promoting charge extraction through better band alignment at the CTL/perovskite interface and improving the asymmetric charge transport due to gradient distribution of CsBr in the perovskite bulk. It is, therefore, very important to have an in-depth understanding of the effect of CsBr on the microstructural and optoelectronic properties of perovskite film as well as the long-term stability of the ensuing PSCs. Furthermore, a suitable, low-cost, and scalable CsBr deposition approach needs to be sought since CsBr has limited solubility in most solvents.

Herein, we present a novel Cs incorporation process where a thin layer of CsBr is thermally evaporated between lead (II) iodide (PbI₂) and organic components. In other words, the perovskite film is formed via a three-step process where PbI₂ is first deposited followed by thermal evaporation of CsBr and finally the organic mixed solution (FAI, MABr, MACl). The effect of the CsBr layer thickness on the microstructural properties, surface chemical states, and electronic structure of the perovskite film is studied. The thickness of the CsBr layer was varied from 0 (control), 30, 50, to 100 nm, and the different perovskite films were labeled CsBr0, CsBr30, CsBr50, and CsBr100, respectively. We see an improvement in the crystal quality and the surface properties of the perovskite films, with the incorporation of CsBr. The resulting PSCs based on the CsBr50 perovskite film showed 15% improvement in PCE and were able to retain over 70% of their PCEs for over 120 days in an unencapsulated state. The results of this study demonstrate the importance of the thermally evaporated CsBr layer in improving the long-term stability of PSCs.

II. MATERIALS AND METHODS

A. Materials

Materials used in this work were purchased from Sigma-Aldrich, and they were used as received unless otherwise indicated. Chemicals include lead (II) iodide (PbI₂, 99.99%), methyl ammonium bromide (MABr), methyl ammonium chloride (MACl), formamidinium iodide (FAI), cesium bromide

(CsBr), titanium diisopropoxide bis(acetylacetonate) (75 wt. % in isopropanol), 2,2',7,7'-tetrakis(*N,N*-di-*p*-methoxyphenylamine)-9,9-spirobifluorene (Spiro-OMeTAD); Fullerene-C60, 4-*tert*-butylpyridine (*t*BP), lithium bis-(*tri*-fluoromethanesulfonyl)imide (Li-TSFI), and tin (IV) oxide nano-particle ink (2.5 wt. % in butanol). Fluorine-doped tin oxide (FTO)-coated glass and solvents such as acetonitrile (99.8%), acetone, isopropyl alcohol (IPA), *N,N*-dimethylformamide (DMF, 99.8%), dimethyl sulfoxide (DMSO, 99.9%), chlorobenzene, and butanol solvents were also purchased from Sigma-Aldrich, while pure gold (99.999%, Lesker) was purchased from Kurt J. Lesker Company.

B. Materials processing

Pre-patterned FTO-coated glass substrates were cut into dimensions of $12.5 \times 25 \text{ mm}^2$ and sequentially cleaned in an ultrasonic bath using detergent, deionized water, acetone, and IPA for 15 min each. The substrates were dried in nitrogen gas before being treated with UV ozone for 15 min to remove any residual organic matter. A compact electron transport layer (ETL) was formed from precursor solutions consisting of 0.15 and 0.3M solutions of TiO_2 as described elsewhere.⁴⁰ However, the 0.3M TiO_2 solution was modified with SnO_2 nanoparticles to obtain SnO_2 - TiO_2 mixed solutions with a volume fraction of 0.2 before being spin coated. The perovskite film was processed via a three-step deposition process where PbI_2 was first spin coated on the ETL, followed by thermal evaporation of CsBr and a final spin coating of the organic components. The PbI_2 was spin coated at 1500 rpm for 30 s from a precursor solution containing 599.3 mg of PbI_2 in 1 ml of DMF: DMSO (19:1, v/v), followed by annealing at 70°C for 1 min. Different thicknesses of CsBr were then deposited onto the PbI_2 thin film using a thermal evaporator (Edward E306A, UK). It is important to note that the deposition of CsBr on the PbI_2 thin film was not immediate due to the waiting period for high vacuum to build after loading the samples in the thermal evaporator.

Subsequently, the organic solution containing a mixture of FAI, MABr, and MAcl (60, 6, and 6 mg) in 1 ml of IPA was spin coated onto CsBr at 1300 rpm for 30 s. This was then annealed at 130°C for 20 min to allow for the formation of perovskite crystals. A layer of the hole transport layer (HTL) was formed by spin coating Spiro-OMeTAD solution onto the perovskite film at 4000 rpm for 30 s. The Spiro-OMeTAD solution was prepared by adding $30 \mu\text{l}$ of *t*BP and $35 \mu\text{l}$ of a solution containing 260 mg of Li-TSFI salt in 1 ml of acetonitrile into a solution containing 72 mg of Spiro-OMeTAD in 1 ml of chlorobenzene. Finally, a 90 nm thick layer of gold was thermally evaporated onto the Spiro-OMeTAD film under a high vacuum (pressure of $\sim 10^6$ Torr) at an average deposition rate of 1.1 \AA/s . All depositions were done under an ambient condition (~ 25 to 30°C , 25%–55% RH).

C. Materials characterization

The microstructural studies of the films were carried out by taking their top view images using a field emission scanning electron microscope (SEM) (JEOL JSM-700F, Hollingsworth & Vose, MA, USA). The structural properties were probed using an x-ray diffractometer (Malvern PANalytical, Westborough, MA, USA) under a $\text{Cu K}\alpha$ radiation source with 2θ angles from 5° – 70° . The optical

properties were measured in the wavelength range of 200–1100 nm using an Ultraviolet–Visible (UV–Vis) spectrometer (AVANTES StarLine, Avaspec-2048), while the photoluminescence (PL) measurement was done with an excitation wavelength of 450 nm using laser light. The X-Ray Photoelectron Spectroscopy (XPS) and Ultraviolet Photoelectron Spectroscopy (UPS) studies were carried out using a PHI5600 XPS system following the method described in Ref. 41. The PV performance and Electrochemical Impedance (EI) characteristics of the fabricated PSC devices were studied under an AM1.5G illumination of 100 mW/cm^2 using a Keithley 2400 source meter unit (Keithley, Tektronix, Newark, NJ, USA) and a potentiostat (SP-300, BioLogic Instrument) each connected to a solar simulator (Oriel, Newport Corporation, Irvine, CA, USA). The J – V measurement for the PSC device was carried out on a device area of 0.1 cm^2 with a voltage scan range of -0.4 to 1.2 V , while the EI studies were performed with an AC amplitude of 10 mV in the frequency range 1 MHz–10 Hz.

III. RESULTS AND DISCUSSION

The morphology of the perovskite film is controlled by its crystallization dynamics, which is a function of many variables, such as perovskite stoichiometry, fabrication conditions, and post-treatment techniques.^{42,43} Proper control of perovskite film morphology is the best route to achieve a compact and pinhole-free film that have better light absorption and longer charge carrier diffusion lengths. Figures 1(a)–1(d) present the SEM images of the perovskite films for different thicknesses of CsBr layers. We observe a change in the morphology of perovskite films with the incorporation of CsBr, which implies that the thickness of the CsBr layer affected their crystallization dynamics. The top surface SEM image of the CsBr0 film shows more pronounced grain boundaries when compared to the CsBr-modified perovskite films. The CsBr30 and CsBr50 show surfaces with no distinct boundaries between adjacent grains, while the CsBr100 shows some grain boundaries, but they are not as pronounced as those of CsBr0. This shows that the CsBr-modified perovskite films had more compact films with well-passivated grain boundaries. This grain boundary passivation effect of CsBr is important in addressing the problems in PSCs that are caused by the presence of defects.

The structural properties of the perovskite films were also studied to gain an understanding on the possible effects of the CsBr layer on their crystal quality. The XRD patterns of the CsBr0, CsBr30, CsBr50, and CsBr100 perovskite films are depicted in Figs. 2(a) and 2(b). All the films showed diffraction peaks at 2θ angles around 14.0° , 19.9° , 24.4° , 28.2° , 31.5° , 40.2° , and 42.8° , showing the formation of the black (alpha) perovskite phase.⁴⁴ The intensities of the main peaks at 14.0° and 28.2° were found to increase with the thickness of the CsBr doping layer up to 50 nm and decreased thereafter. The increase in peak intensities between CsBr0 and CsBr50 shows that the CsBr layer up to 50 nm improves the crystallinity of the perovskite film. Beyond 50 nm, the crystallinity decreases slightly as seen by the reduction in the intensity of the main peak. It is also evident from Fig. 2(b) that the major peak at 14.0° shifts toward higher angles as the thickness of the CsBr layer increases, indicating a decrease in the lattice parameter. This decrease in the lattice parameter is a confirmation that Cs, which

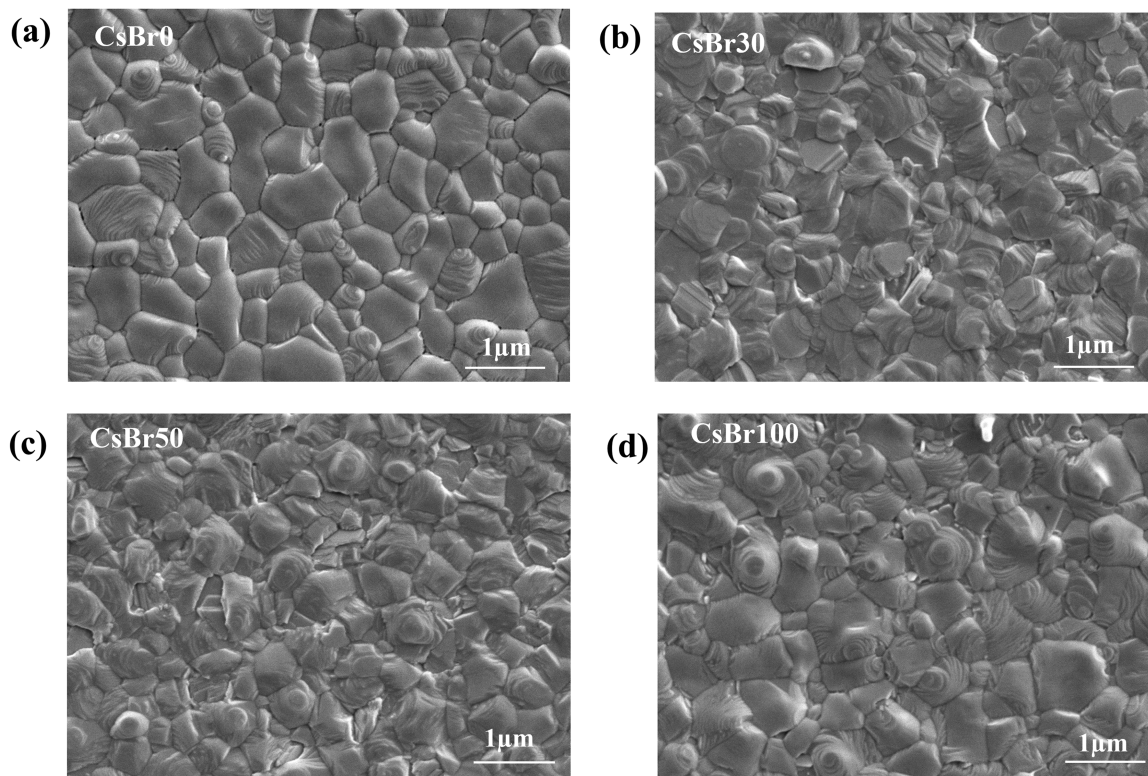


FIG. 1. SEM images of perovskite films at different thicknesses of CsBr layers: (a) control, (b) 30, (c) 50, and (d) 100 nm.

has a smaller ionic radius, has successfully been incorporated into the perovskite film. Figure 2(c) shows the variation of the position and d-spacing of the major peak at 14.0° with the thickness of the CsBr layer. In agreement with the shift in the peak position to higher angles, the d-spacing decreases as the thickness of the CsBr layer increases. The peak seen at 12.6° in the perovskite films CsBr0 and CsBr30 can be indexed to the (001) plane of hexagonal lead iodide (PbI_2).⁴⁵ The presence of this peak in these films shows the existence of some unreacted lead iodide. The intensity of this peak is

lower in the perovskite film CsBr30 when compared to that in the CsBr0 film and is invisible in the films CsBr50 and CsBr100. This shows that the presence of the CsBr layer is likely to have facilitated the reaction of PbI_2 with the organic components to form perovskite.

The surface chemistry of a semiconductor is quite sensitive to the fabrication conditions and the presence of any substance that may induce changes in the lattice discontinuities and periodicity of chemical bonds.⁴⁶ A change in the surface states of the perovskite

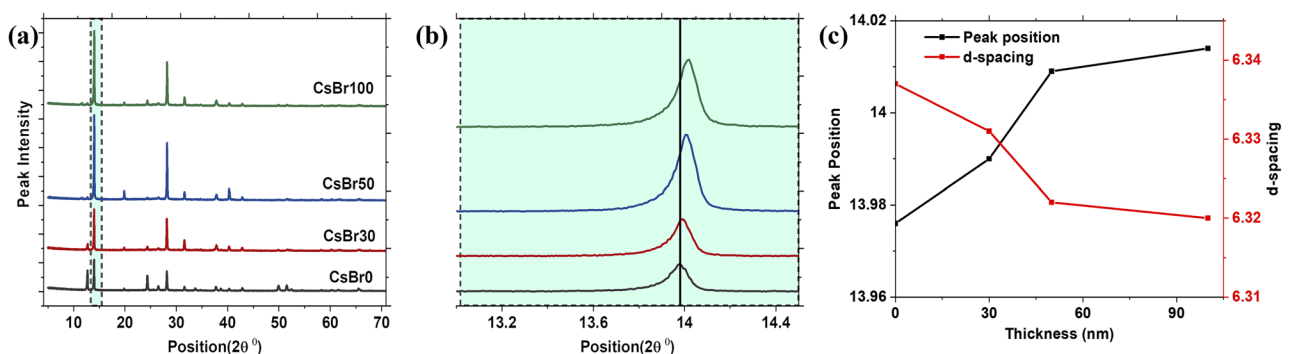


FIG. 2. (a) XRD patterns of the perovskite films with different CsBr layer thicknesses. (b) Zoomed-in view of the major peak. (c) Variation of peak position and d-spacing with the thickness of the CsBr layer.

film affects its electronic structure and its interfacial interaction with adjacent CTLs, which influences its charge transport dynamics.^{47,48} To understand the influence of CsBr on the surface states of the perovskite films, x-ray photoelectron spectroscopy study of the different films was carried out. The XP results complemented the XRD results by revealing near-interfacial concentration changes in the perovskite films as a function of CsBr deposition thickness. For perovskites with 0, 30, 50, and 100-nm-thick initial CsBr layers, Fig. 3 presents the high-resolution XP spectra of the Cs $3d_{5/2}$ regions that are each normalized to the corresponding I $3d_{5/2}$ feature intensity. The full survey XP spectrum for each of the studied perovskite films is presented in Fig. S1 in the supplementary material. Figure 3 demonstrates that thicker CsBr films yield successively increasing relative concentrations of Cs⁺ cations in the near-interfacial region of the resulting perovskite films. This indicates that varying the thickness of the CsBr

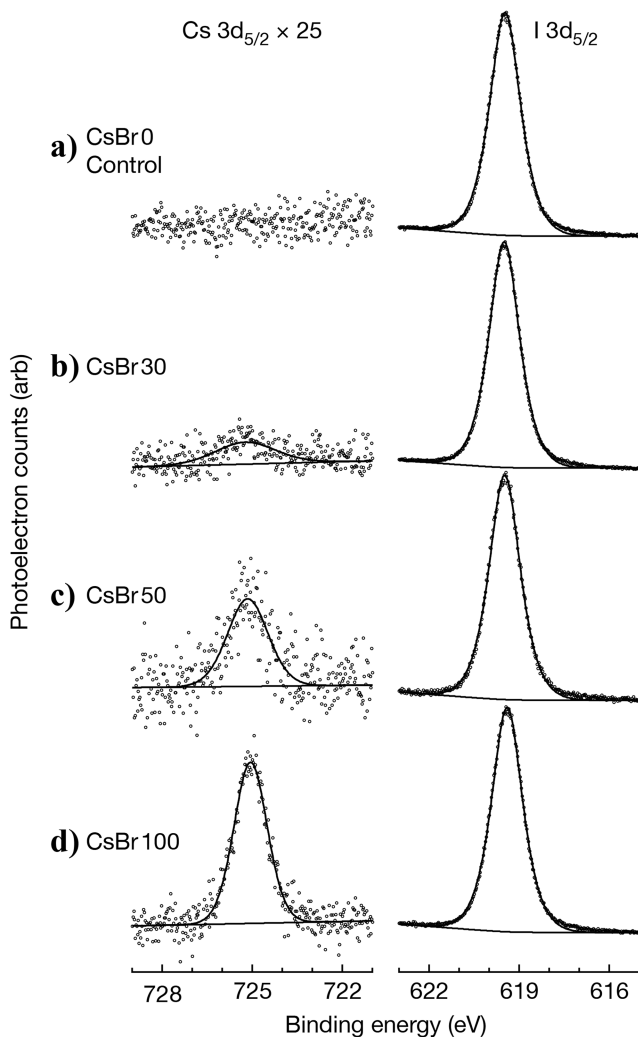


FIG. 3. High-resolution XP spectra of the Cs $3d_{5/2}$ and I $3d_{5/2}$ regions for perovskite samples as a function of CsBr thickness: (a) control, (b) 30, (c) 50, and (d) 100 nm.

layer effectively regulates the amount of Cs that can diffuse toward the surface of the perovskite film. The atomic mass ratios of different elements at the surface of the films CsBr0, CsBr30, CsBr50, and CsBr100 were determined from their XP core level spectra and tabulated in Table S1. The atomic mass ratios of Cs to I and Cs to oxidized Pb at the surface of the perovskite film were found to increase with the thickness of the CsBr layer. This is a clear indication that the concentration of Cs at the surface increased with the thickness of the CsBr layer. We also employed the Energy Dispersive X-ray Spectroscopy (EDS) cross-sectional analysis to study the distribution of Cs and Br within the bulk of the perovskite films and the underlying components.

The EDS cross-sectional maps of the CsBr30- and CsBr100-modified perovskite films are displayed in Fig. S2 in the supplementary material. The maps reveal the presence of Cs and Br in the bulk of the perovskite films and some traces of Cs and Br were also detected in the components below the perovskite films, possibly due to diffusion that occur during annealing.⁴⁰

The perovskite active layer is the most important component of PSC due to its intrinsic function of light absorption and photogeneration. The light absorption capability of the perovskite film determines the number of photons that can be absorbed to generate the charge carriers and is usually influenced by its thickness, defect density state, and bandgap.^{49,50} To understand the effects of the CsBr layer on the photophysical properties of perovskite films, we carried out UV-Vis and PL studies on the different films. Figure 4(a) shows the light absorption spectra of the perovskite films at different thicknesses of CsBr. We observe a small blueshift in the absorption onset of the perovskite films as the CsBr layer thickness increases, which signifies an increase in the optical bandgap. The bandgap of the perovskite film at different CsBr thickness was estimated from absorbance using the Tauc plot, as shown in Fig. 4(b). The mean values of the bandgap were slightly blueshifted from 1.547 ± 0.015 to 1.565 ± 0.021 eV as the thickness of the CsBr layer increased from 0 to 100 nm, which is also evident in the shift in the normalized PL peaks shown in Fig. 4(c). The shift in bandgap could be an indication of changes in the electronic band structure or reduction in the band tail states of the perovskite films with increasing CsBr layer thickness.

The distribution of band tail states within the bandgap of the perovskite film can be studied by estimating the Urbach energy (E_u), a parameter that indicates the level of structural disorder in the film.⁵¹ The E_u values of the different perovskite films were determined from the inverse slope of a plot of $\ln \alpha$ vs photon energy ($h\nu$) (see Fig. S3). The calculated values of E_u were observed to decrease from 19.24 ± 1.28 meV for CsBr0 to 16.67 ± 2.44 meV for CsBr50 but thereafter increased to 19.74 ± 1.32 meV for CsBr100 perovskite films [Fig. 4(d)]. The lower E_u values for CsBr30 and CsBr50 films signify a decrease in structural disorder in these perovskite films.⁵² The relative position of the band edges is also important in the charge injection and extraction dynamics in PSC devices since it controls the band offsets at the interface with the CTLs.⁵³ To investigate the impact of the CsBr layer on the electronic band structure of perovskite films, we carried out a UPS study on the different perovskite films. Figure S4 shows the variation of the secondary photoemission cut-off energies (E_{SEC}) for CsBr0, CsBr30, CsBr50, and CsBr100 perovskite films. Figure S4 shows that E_{SEC} values shifted toward lower binding energies as the CsBr layer thickness increased

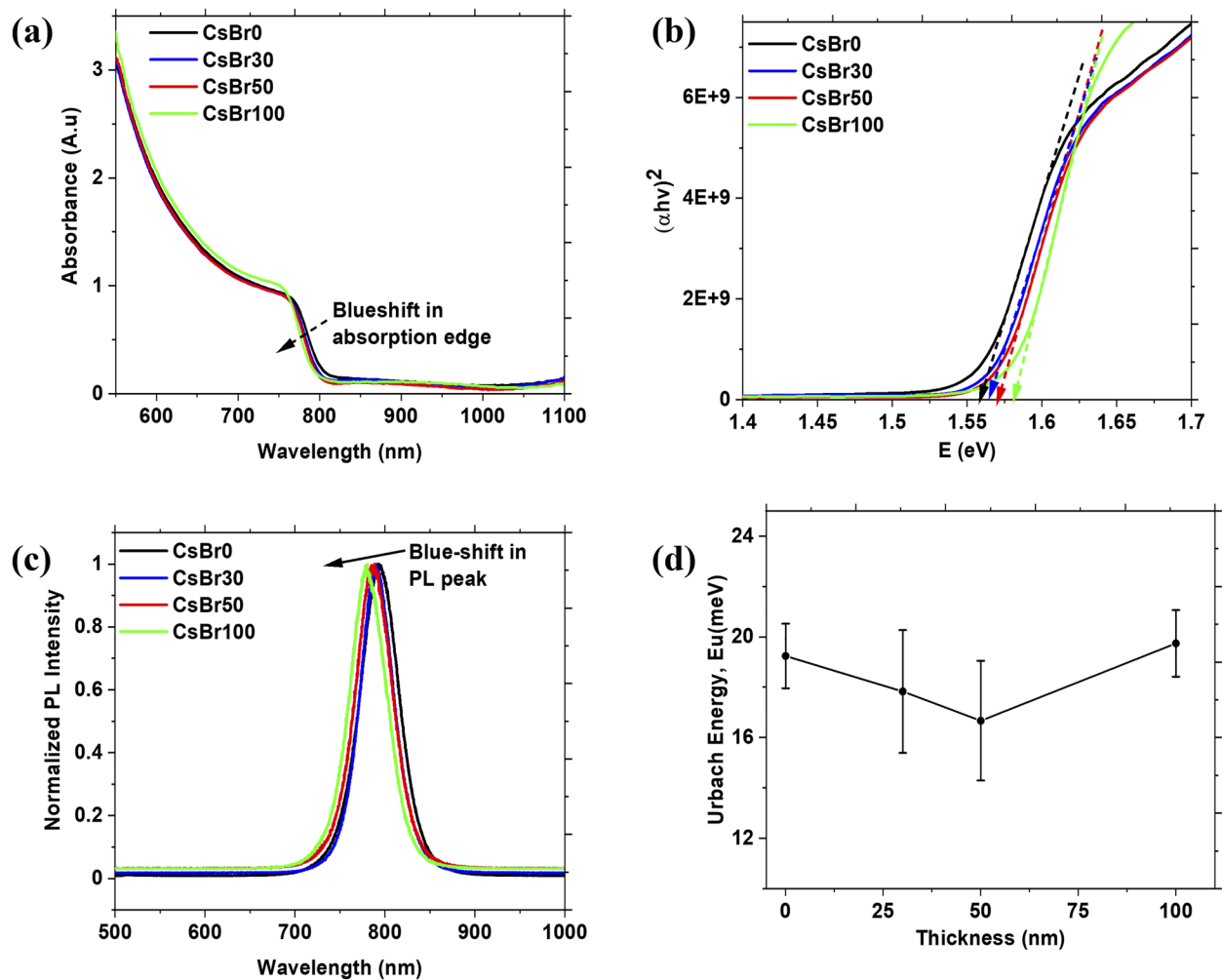


FIG. 4. (a) Absorption spectra of perovskite films, (b) Tauc plot, (c) normalized PL curves, and (d) E_u values of the different perovskite films.

from 0 to 50 nm and shifted toward higher binding energies thereafter. This led to a slight increase in the work function (Φ_{WF}) of the top surface of the perovskite films from 3.95 eV for CsBr0 to 4.12 eV for CsBr50 and later decreased to 3.99 eV for CsBr100. The increase in the Φ_{WF} of the surface of the perovskite film signifies a downward shift in the Fermi level (E_f), which may arise due to the reduction in the donor-type defect states, such as iodine vacancies or Pb^0 , that are known to make the films exhibit n-type conductivity.⁵⁴

The electronic band edge positions were determined from the combined UPS and UV-Vis data for the different perovskite films. Table S2 summarizes the experimentally determined and interpreted values of Φ_{WF} and the band edge positions relative to the vacuum level (E_{vac}). The details of how these parameters were obtained are given in the [supplementary material](#). From these values, we drew the electronic band structure of the different perovskite films as depicted in Fig. 5(a). The figure indicates that the CsBr layer thickness played a role in tuning the band edge positions in the

perovskite film, which control the interfacial band alignment and the charge carrier injection dynamics of the ensuing PSC structure shown in Fig. 5(b). Higher interfacial band offsets between the perovskite layer and the CTL may cause thermionic power losses that contribute to the reduction in V_{oc} .⁵⁵ Considering the planar PSC architecture we fabricated, the downward shift in E_{CBM} of the perovskite film with CsBr thickness leads to a reduction in the interfacial energy barrier at the ETL/perovskite interface, which favors electron injection.

The performance of PSC is a function of many variables that are strongly influenced by the device fabrication conditions.⁵⁶ To understand the impacts of the thermally evaporated CsBr layer on the PV parameters, we recorded the J-V curves of the PSCs fabricated with CsBr0, CsBr30, CsBr50, and CsBr100 perovskite films as absorber layers. Figure 6(a) compares the J-V curves of the control and the best performing CsBr-modified PSC devices from which we observe an improvement in both the short circuit current (J_{sc}) and the open circuit voltage (V_{oc}) in the CsBr-modified device. The J-V

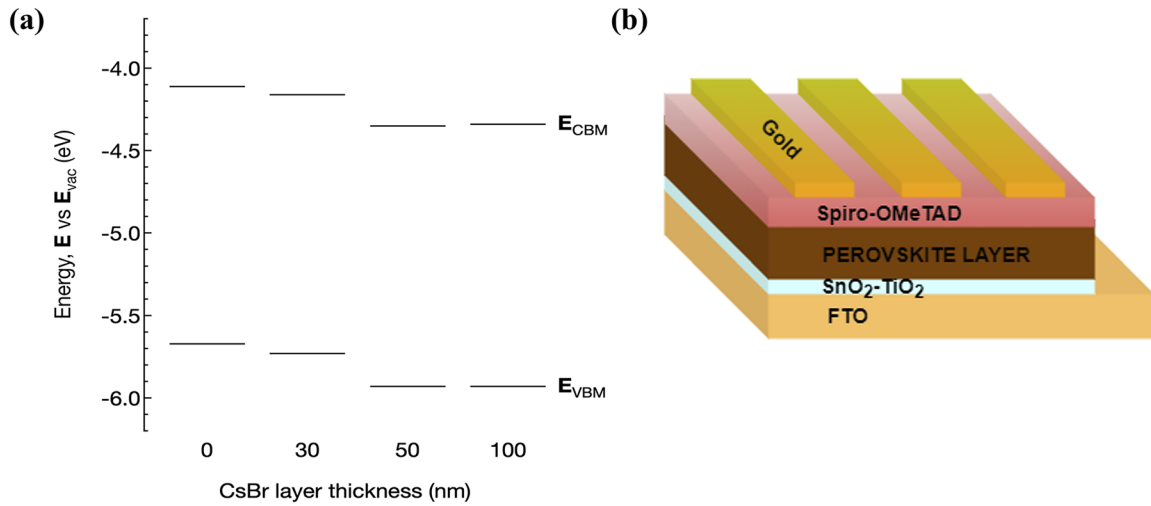


FIG. 5. (a) Band structure of perovskite films at different CsBr thicknesses and (b) schematic of the fabricated planar PSC.

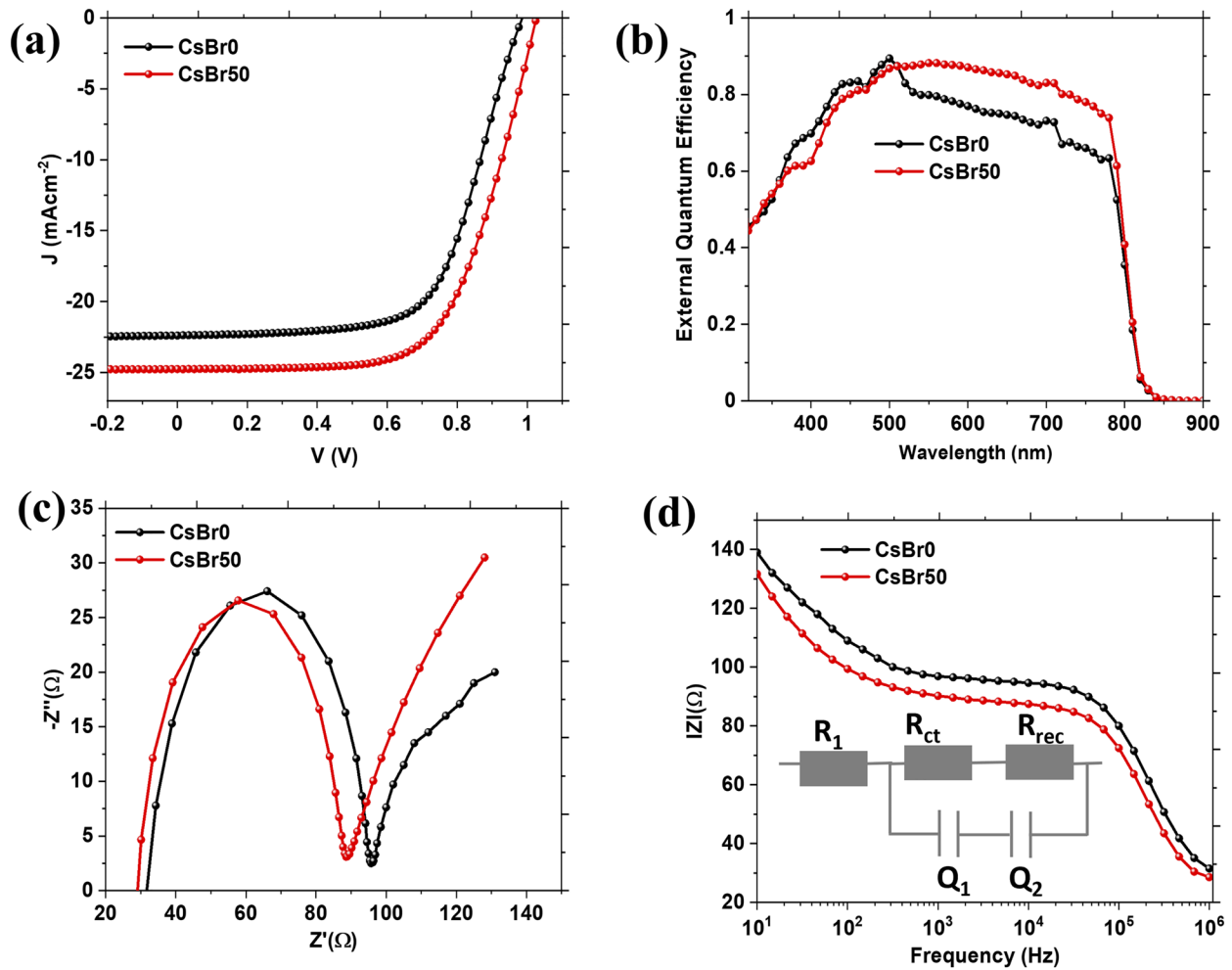


FIG. 6. (a) J-V curves, (b) EQE curves, (c) Nyquist plots, and (d) Bode plots for control and best performing PSCs.

curves for the different PSCs are depicted in Fig. S4, while their corresponding PV performance parameters are summarized in Table S3. It is seen that the PV performance parameters of the different PSCs varied with the thickness of the CsBr layer in the active layer. The PSC device with the CsBr50 perovskite film showed a better PCE when compared to the rest. The improved PCE for the device with the CsBr50 perovskite film as the absorber layer can be associated with the improved perovskite film morphology or better interface band alignment that led to improved charge carrier collection efficiency as shown by the external quantum efficiency (EQE) curves in Fig. 6(b).

To establish the real cause of the observed PCE improvement in the PSC device with the CsBr50 perovskite absorber, we probed the charge transport and recombination dynamics of the device relative to the control device using EI spectroscopy. The EI spectra for both PSC devices were represented in the form of Nyquist and Bode plots,

as shown in Figs. 6(c) and 6(d). The plots indicate that the devices exhibit two relaxation processes that are usually associated with charge transport dynamics. In the Nyquist plots of Fig. 6(c), we see two arcs, one in the low frequency regime and the other in the high frequency regime, which are, respectively, associated with recombination and charge carrier transfer resistances within the layered PSC structure.⁵⁷ The Nyquist plots were fitted with an equivalent circuit consisting of resistors and constant phase elements, shown in the inset of Fig. 6(d), in order to obtain the values of the parameters of interest, such as the series resistance (R_1) and the charge transfer resistance (R_{ct}). The values of R_1 were determined to be 34.12 and 33.46 Ω for the control and CsBr-modified PSC devices, respectively, while the R_{ct} values were 66.84 and 62.02 Ω . Thus, R_1 and R_{ct} values were lower for the CsBr-modified PSC device when compared to the control device, which led to the reduction in charge carrier recombination.

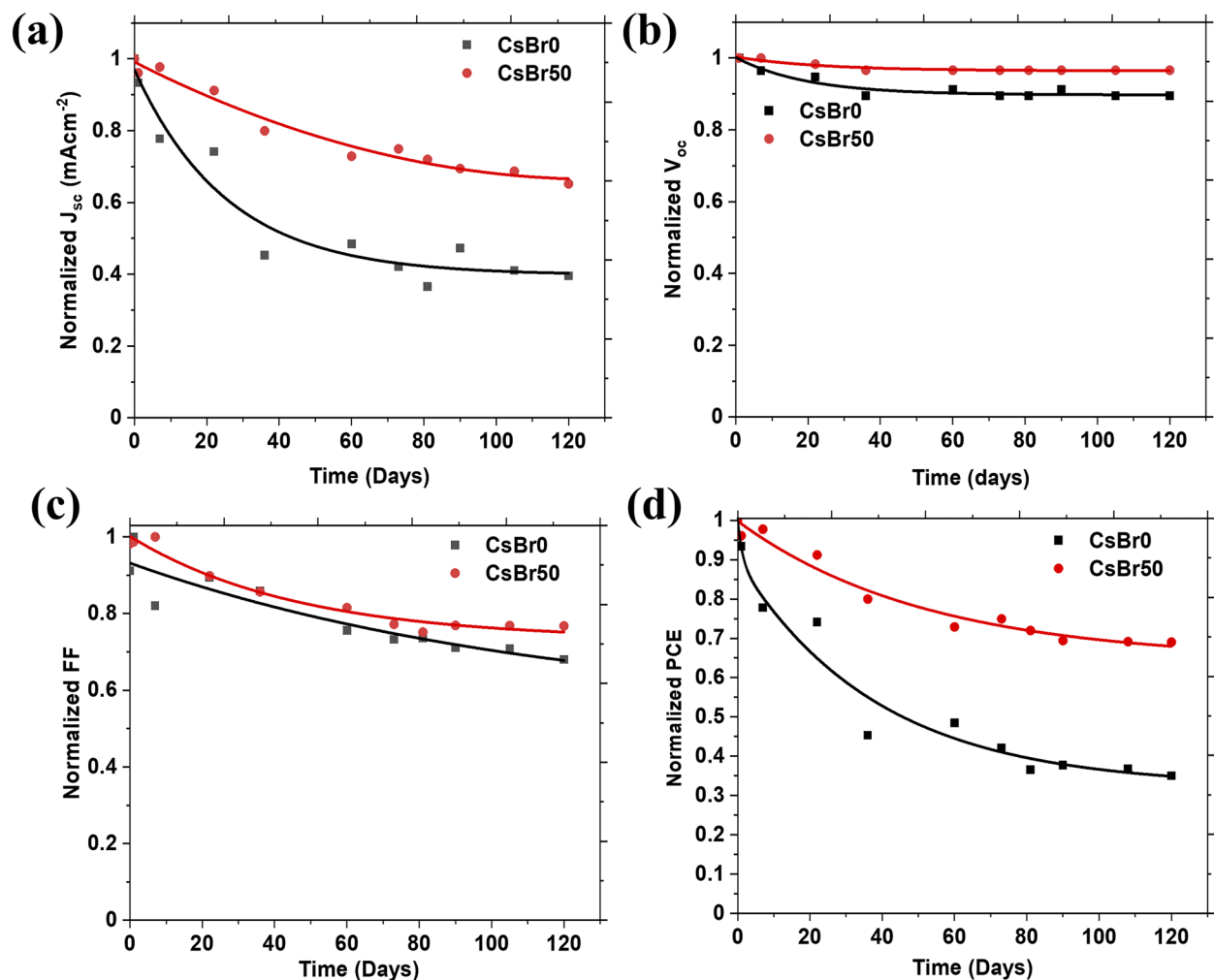


FIG. 7. Variation in PV performance parameters of PSC with time: (a) normalized current density (J_{sc}), (b) normalized open circuit voltage (V_{oc}), (c) normalized fill factor (FF), and (d) normalized PCE.

The long-term stability of PSCs under ambient conditions is another important parameter for consideration in the effort to accelerate the commercialization of this PV technology. To understand the role of the CsBr layer on the degradation behavior of PSCs, we monitored the PV performance characteristics of the control and the best performing CsBr-modified PSC devices left to age in an unencapsulated state for a period of 4 months under ambient conditions by periodically recording their J–V and EQE curves. The PV parameters were determined from the J–V curves and normalized to clearly show their degradation rate. The evolution of the normalized PV performance parameters with time (days) is depicted in

Figs. 7(a)–7(d). The figure shows that the PV performance parameters of the control and best performing PSC based on the CsBr50 perovskite absorber decreased gradually with time. It is important to note that the decrease in the PV parameters of the PSC device with the CsBr-modified absorber layer was slower than that of the control device. The PSC with the CsBr50 perovskite film as the light absorbing layer was able to retain over 70% of its PCE for over 120 days.

The EQE of a solar cell is a parameter that quantifies the charge carrier collection efficiency of the device at a given wavelength region of the solar spectrum and provides useful information

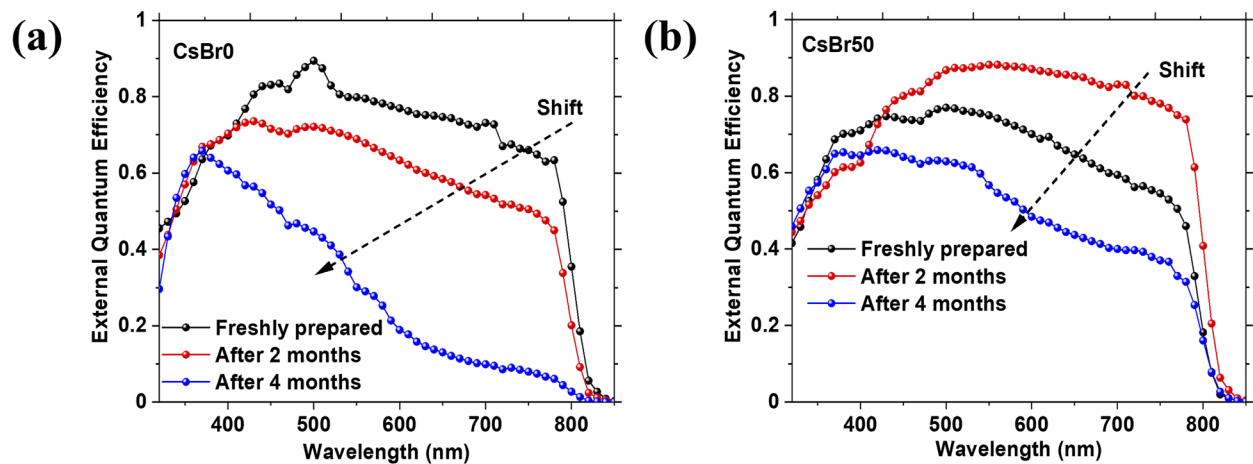


FIG. 8. EQE curves of (a) the control and (b) best performing CsBr-modified PSC at different times.

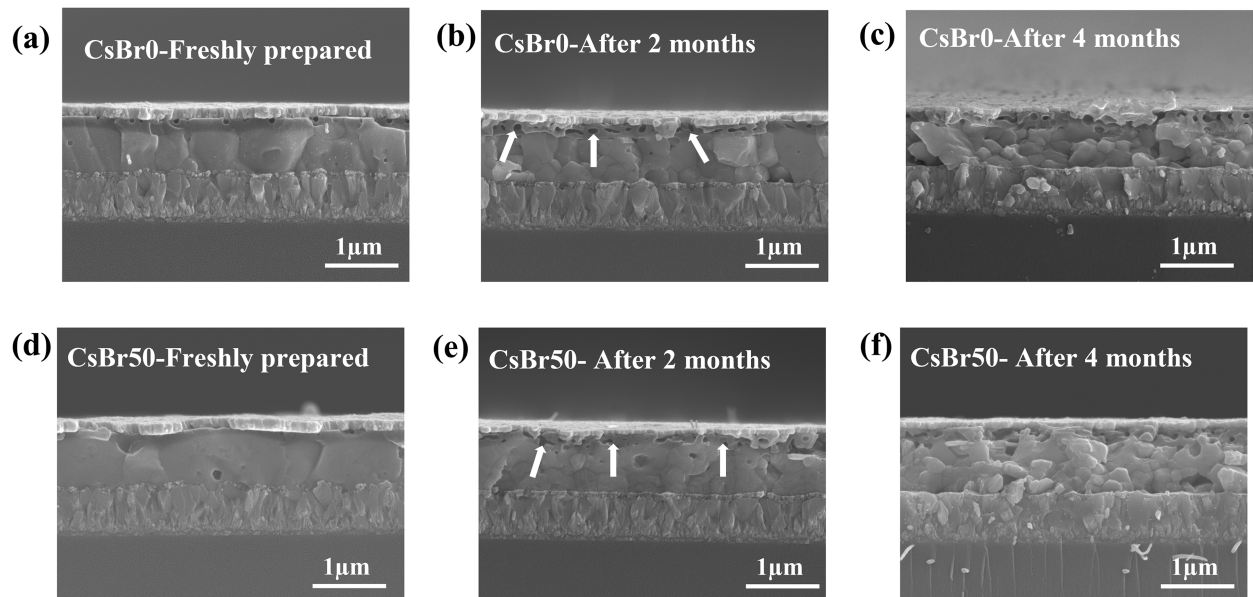


FIG. 9. SEM cross-sectional images of PSCs at different aging times: (a) freshly prepared CsBr0, (b) CsBr0 film after 2 months, (c) CsBr0 film after 4 months, (d) freshly prepared CsBr50, (e) CsBr50 film after 2 months, and (f) CsBr50 film after 4 months.

on the degradation behavior of PSCs.⁵⁸ Figures 8(a) and 8(b) depict the EQE curves of the control and best performing CsBr-modified PSCs. From the figure, we observe that the EQEs of both PSC devices decreased with the aging time and that the decrease is more pronounced in the long wavelength region of the solar spectrum. The decrease in the EQE is also seen to be faster for the control device than that of the CsBr-modified counterpart. The faster EQE decay in the long wavelength region is an indication that the charge carrier collection from the bulk and at the back surface of the devices is impaired as they age.^{58,59} This means that the charge transfer properties at the perovskite/Spiro-OMeTAD interface become poor as the devices age. To establish the real cause of this observation, we compared the SEM cross-sectional images of freshly prepared devices and those that have been aged for 2 and 4 months under ambient conditions for both the control and the CsBr-modified PSC devices. Figures 9(a)–9(f) show the SEM images from which we observe voids (marked with arrows) in the Spiro-OMeTAD (HTL) in both the control and CsBr-modified devices after being aged. This shows that the HTL undergoes degradation faster than the other components of the device possibly because it is more exposed to the ambient conditions when compared to the other components. The degradation in the Spiro-OMeTAD will affect the interfacial energetics at the perovskite/HTL interface of PSC, which reduces the charge carrier collection efficiency. The degradation of Spiro-OMeTAD will finally expose the perovskite layer to the ambient conditions, making it to degrade as seen in the SEM cross-sectional images after aging the devices for a period of 4 months. The perovskite film CsBr0 appears to be degraded more than the perovskite film CsBr50 for the CsBr-modified device. This shows that the CsBr layer has an important effect of suppressing the degradation of PSCs.

IV. CONCLUSION

A thermally evaporated CsBr layer of appropriate thickness in a FA-rich perovskite film passivates the grain boundaries and modifies the interfacial energetics with adjacent CTLs. This improves the charge transport and PV performance characteristics of PSC while simultaneously suppressing the degradation of the perovskite layer when exposed to ambient conditions. We have shown that the incorporation of a 50 nm thick CsBr layer in the absorber layer helps improve the PCE and long-term stability of PSC. The CsBr-modified PSC showed a 15% improvement in the PCE when compared to the control device and was able to retain about 70% of its initial PCE for over 120 days. The improvement in PCE and stability resulted from defect passivation and band structure modulation effects of CsBr as revealed by the SEM and UPS studies.

SUPPLEMENTARY MATERIAL

See the [supplementary material](#) for the summary of the elemental analysis, the electronic band structure parameters of the perovskite films at different CsBr thicknesses, and the corresponding PV performance parameters of the fabricated PSC devices.

ACKNOWLEDGMENTS

The authors wish to acknowledge the PASET-RSIF and World Bank for their financial support and Worcester Polytechnic Institute

for providing research facilities that contributed immensely to the success of this research work.

DATA AVAILABILITY

The data that support the findings of this study are available from the corresponding author upon reasonable request.

REFERENCES

- 1 Z. Shi and A. H. Jayatissa, *Materials* **11**, 36 (2018).
- 2 A. M. Khalaji, S. Bakhoda, R. Saidur, and H. Hanaei, *Renewable Sustainable Energy Rev.* **81**, 2812 (2018).
- 3 Q. Tai, K. C. Tang, and F. Yan, *Energy Environ. Sci.* **12**, 2375 (2019).
- 4 M. A. Green, Y. Hishikawa, E. D. Dunlop, D. H. Levi, J. Hohl-Ebinger, and A. W. Y. Ho-Baillie, *Prog. Photovoltaics* **26**, 3 (2018).
- 5 L. Chouhan, S. Ghimire, C. Subrahmanyam, T. Miyasaka, and V. Biju, *Chem. Soc. Rev.* **49**, 2869 (2020).
- 6 I. Hussain, H. P. Tran, J. Jaksik, J. Moore, N. Islam, and M. J. Uddin, *Emergent Mater.* **1**, 133 (2018).
- 7 S. Kundu and T. L. Kelly, *EcoMat* **2**, e12025 (2020).
- 8 Q. Wali, F. J. Iftikhar, M. E. Khan, A. Ullah, Y. Iqbal, and R. Jose, *Org. Electron.* **78**, 105590 (2020).
- 9 M. I. Asghar, J. Zhang, H. Wang, and P. D. Lund, *Renewable Sustainable Energy Rev.* **77**, 131 (2017).
- 10 L. Fu, H. Li, L. Wang, R. Yin, B. Li, and L. Yin, *Energy Environ. Sci.* **13**, 4017 (2020).
- 11 B. Chen, M. Yang, S. Priya, and K. Zhu, *J. Phys. Chem. Lett.* **7**, 905 (2016).
- 12 H. S. Kim, A. Hagfeldt, and N. G. Park, *Chem. Commun.* **55**, 1192 (2019).
- 13 R. Liu and K. Xu, *Micro Nano Lett* **15**, 349 (2020).
- 14 J. Yakianggam, S. Monnoi, P. Ruankham, A. Intaniwet, and S. Choopun, *Mater. Today Proc.* **17**, 1210–1216 (2019).
- 15 F. Zhang and K. Zhu, *Adv. Energy Mater.* **10**, 1902579 (2019).
- 16 W. Zeng, X. Liu, X. Guo, Q. Niu, J. Yi, R. Xia, Y. Min, Y. Kim, and H. Kim, *Molecules* **22**, 540 (2017).
- 17 S. Xiao, Y. Li, S. Zheng, and S. Yang, *MRS Bull.* **45**, 431 (2020).
- 18 G. Landi, H. C. Neitzert, C. Barone, C. Mauro, F. Lang, S. Albrecht, B. Rech, and S. Pagano, *Adv. Sci.* **4**, 1700183 (2017).
- 19 T. S. Sherkar, C. Mombalona, L. Gil-Escrig, J. Ávila, M. Sessolo, H. J. Bolink, and L. J. A. Koster, *ACS Energy Lett.* **2**, 1214 (2017).
- 20 T. Wang, Z. Cheng, Y. Zhou, H. Liu, and W. Shen, *J. Mater. Chem. A* **7**, 21730 (2019).
- 21 N. K. Tailor, M. Abdi-Jalebi, V. Gupta, H. Lu, M. I. Dar, G. Li, and S. Satapathi, *J. Mater. Chem. A* **8**, 21356 (2020).
- 22 C. Yi, J. Luo, S. Meloni, A. Boziki, N. Ashari-Astani, C. Gratzel, S. M. Zakeeruddin, U. Rothlisberger, and M. Gratzel, *Energy Environ. Sci.* **9**, 656 (2016).
- 23 Z. Li, M. Yang, J.-S. Park, S.-H. Wei, J. J. Berry, and K. Zhu, *Chem. Mater.* **28**, 284 (2016).
- 24 J. Xu, C. C. Boyd, Z. J. Yu, A. F. Palmstrom, D. J. Witter, B. W. Larson, R. M. France, J. Werner, S. P. Harvey, E. J. Wolf, W. Weigand, S. Manzoor, M. F. A. M. van Hest, J. J. Berry, J. M. Luther, Z. C. Holman, and M. D. McGehee, “Triple-halide wide-band gap perovskites with suppressed phase segregation for efficient tandems,” *Science* **364**, 1097 (2020).
- 25 T. Liu, H. Lai, X. Wan, X. Zhang, Y. Liu, and Y. Chen, *Chem. Mater.* **30**, 5264 (2018).
- 26 S. Tang, S. Huang, G. J. Wilson, and A. Ho-Baillie, *Trends Chem.* **2**, 638 (2020).
- 27 F. Bella, P. Renzi, C. Cavallo, and C. Gerbaldi, *Chem. - Eur. J.* **24**, 12183 (2018).
- 28 C. W. Myung, J. Yun, G. Lee, and K. S. Kim, *Adv. Energy Mater.* **8**, 1702898 (2018).
- 29 C. Li, X. Lu, W. Ding, L. Feng, Y. Gao, and Z. Guo, *Acta Crystallogr., Sect. B: Struct. Sci.* **64**, 702 (2008).
- 30 R. Prasanna, A. Gold-Parker, T. Leijtens, B. Conings, A. Babayigit, H. G. Boyen, M. F. Toney, and M. D. McGehee, *J. Am. Chem. Soc.* **139**, 11117 (2017).

- ³¹K. A. Bush, K. Frohna, R. Prasanna, R. E. Beal, T. Leijtens, S. A. Swifter, and M. D. McGehee, *ACS Energy Lett.* **3**, 428 (2018).
- ³²M. Saliba, T. Matsui, J.-Y. Seo, K. Domanski, J.-P. Correa-Baena, M. K. Nazeeruddin, S. M. Zakeeruddin, W. Tress, A. Abate, A. Hagfeldt, and M. Grätzel, *Energy Environ. Sci.* **9**, 1989 (2016).
- ³³Z. Li, J. Xu, S. Zhou, B. Zhang, X. Liu, S. Dai, and J. Yao, *ACS Appl. Mater. Interfaces* **10**, 38183 (2018).
- ³⁴R. D. Chavan, D. Prochowicz, P. Yadav, M. M. Tavakoli, A. Nimbalkar, S. P. Bhoite, and C. K. Hong, *Sol. RRL* **3**, 1900294 (2019).
- ³⁵Y. Xue, J. Tian, H. Wang, H. Xie, S. Zhu, B. Zheng, C. Gao, and X. Liu, *RSC Adv.* **8**, 25645 (2018).
- ³⁶N. Ueoka, T. Oku, Y. Ohishi, H. Tanaka, A. Suzuki, H. Sakamoto, M. Yamada, S. Minami, and S. Tsukada, *AIP Conf. Proc.* **2067**, 020026 (2018).
- ³⁷W. Li, W. Zhang, S. Van Reenen, R. J. Sutton, J. Fan, A. A. Haghighirad, M. B. Johnston, L. Wang, and H. J. Snaith, *Energy Environ. Sci.* **9**, 490 (2016).
- ³⁸S. Chen, J. Dong, J. Wu, S. Hou, J. Xing, H. Liu, and H. Hao, *Sol. Energy Mater. Sol. Cells* **201**, 110110 (2019).
- ³⁹S. Pang, C. Zhang, H. Dong, Z. Zhang, D. Chen, W. Zhu, J. Chang, Z. Lin, J. Zhang, and Y. Hao, *ACS Appl. Mater. Interfaces* **1**, 4991 (2021).
- ⁴⁰D. O. Oyewole, R. K. Koech, R. Ichwani, R. Ahmed, J. H. Tamayo, S. A. Adeniji, J. Cromwell, E. C. Ulloa, O. K. Oyewole, B. Agyei-Tuffour, L. V. Titova, N. A. Burnham, and W. O. Soboyejo, *AIP Adv.* **11**, 065327 (2021).
- ⁴¹A. D. Carl, R. E. Kalan, J. D. Obayemi, M. G. Zebaze Kana, W. O. Soboyejo, and R. L. Grimm, *ACS Appl. Mater. Interfaces* **9**, 34377 (2017).
- ⁴²M. Abbas, L. Zeng, F. Guo, M. Rauf, X. C. Yuan, and B. Cai, *Materials* **13**, 4851 (2020).
- ⁴³F. Guo, S. Qiu, J. Hu, H. Wang, B. Cai, J. Li, X. Yuan, X. Liu, K. Forberich, C. J. Brabec, and Y. Mai, *Adv. Sci.* **6**, 1901067 (2019).
- ⁴⁴X. Dong, D. Chen, J. Zhou, Y.-Z. Zheng, and X. Tao, *Nanoscale* **10**, 7218 (2018).
- ⁴⁵D. Acuña, B. Krishnan, S. Shaji, S. Sepúlveda, and J. L. Menchaca, *Bull. Mater. Sci.* **39**, 1453 (2016).
- ⁴⁶L. K. Ono and Y. Qi, *J. Phys. Chem. Lett.* **7**, 4764 (2016).
- ⁴⁷F. Zu, P. Amsalem, M. Ralaifarisoa, T. Schultz, R. Schlesinger, and N. Koch, *ACS Appl. Mater. Interfaces* **9**, 41546 (2017).
- ⁴⁸S. Shao and M. A. Loi, *Adv. Mater. Interfaces* **7**, 1901469 (2020).
- ⁴⁹B. Wang, K. Y. Wong, S. Yang, and T. Chen, *J. Mater. Chem. A* **4**, 3806 (2016).
- ⁵⁰B. N. Ezealigo, A. C. Nwanya, S. Ezugwu, S. Offiah, D. Obi, R. U. Osuji, R. Bucher, M. Maaza, P. Ejikeme, and F. I. Ezema, *Arab. J. Chem.* **13**, 988 (2020).
- ⁵¹J. Chantana, Y. Kawano, T. Nishimura, A. Mavlonov, and T. Minemoto, *Sol. Energy Mater. Sol. Cells* **210**, 110502 (2020).
- ⁵²V. M. Caselli, Z. Wei, M. M. Ackermans, E. M. Hutter, B. Ehrler, and T. J. Savenije, *ACS Energy Lett.* **5**, 3821 (2020).
- ⁵³C. M. Wolff, F. Zu, A. Paulke, L. P. Toro, N. Koch, and D. Neher, *Adv. Mater.* **29**, 1700159 (2017).
- ⁵⁴L. A. Frolova, N. N. Dremova, and P. A. Troshin, *Chem. Commun.* **51**, 14917 (2015).
- ⁵⁵M. Stolterfoht, P. Caprioglio, C. M. Wolff, J. A. Márquez, J. Nordmann, S. Zhang, D. Rothhardt, U. Hörmann, Y. Amir, A. Redinger, L. Kegelmann, F. Zu, S. Albrecht, N. Koch, T. Kirchartz, M. Saliba, T. Unold, and D. Neher, *Energy Environ. Sci.* **12**, 2778 (2019).
- ⁵⁶P. Roy, N. Kumar Sinha, S. Tiwari, and A. Khare, *Sol. Energy* **198**, 665 (2020).
- ⁵⁷E. J. Juarez-Perez, M. Wußler, F. Fabregat-Santiago, K. Lakus-Wollny, E. Mankel, T. Mayer, W. Jaegermann, and I. Mora-Sero, *J. Phys. Chem. Lett.* **5**, 680 (2014).
- ⁵⁸P. Hierrezuelo-Cardet, A. F. Palechor-Ocampo, J. Caram, F. Ventosinos, D. Pérez-del-Rey, H. J. Bolink, and J. A. Schmidt, *J. Appl. Phys.* **127**, 235501 (2020).
- ⁵⁹L. Xu, L. L. Deng, J. Cao, X. Wang, W. Y. Chen, and Z. Jiang, *Nanoscale Res. Lett.* **12**, 159 (2017).